AAS 24-321

PRELIMINARY DESIGN STRATEGY FOR LONG-TERM LOITERING ORBITS IN CISLUNAR SPACE

Mitchell Dominguez* **and Kathleen C. Howell†**

Cislunar hubs such as the NASA Gateway facility, among others, are designed to interface with visiting spacecraft. Operational considerations, however, inevitably require visitors to loiter while other spacecraft complete their objectives. This investigation introduces an approach for designing long-duration loitering trajectories in the Circular Restricted Three Body Problem (CR3BP) by leveraging the hub orbit center manifold. From the perspective of a linear analysis, the solution space for ballistic loitering orbits under relative distance constraints is characterized. Sample loitering orbits and subsequent rendezvous maneuvers are evaluated near hub orbits with varying stability characteristics, demonstrating general applicability.

INTRODUCTION

With international governmental, commercial, and scientific interest in progressively more complex missions in cislunar space rapidly increasing, the necessity for implementing multi-spacecraft mission architectures is apparent. In-space servicing, assembly, and manufacturing (ISAM), including technologies such as refueling depots, is envisioned as a key component for sustainable cislunar operations.[1] The NASA Gateway concept is a notable example, with a central spacecraft, comprised of multiple components, interfacing with myriad arriving and departing other spacecraft.[2–4] Additionally, future large space telescopes in multibody orbits, e.g., the Large Ultraviolet/Optical/Infrared Surveyor (LUVOIR), are being designed with the potential for servicing.[5] Rendezvous, proximity operations, and docking (RPOD) between two spacecraft in Earth orbit enjoys a rich history.[1] However, in multibody environments, formation flying and relative motion are still relatively new scenarios.

The available literature on formation flying and relative motion in multibody regimes includes investigations that focus on leveraging the natural dynamical structures that arise in the vicinity of periodic orbits. Frequently, the relative motion literature introduces the complexities of designing the motion of a chaser spacecraft moving with respect to a target that is in an established permanent orbit. Elliott and Bosanac introduce the concept of local toroidal coordinates, defined using the complex center subspace associated with periodic orbits, exploiting the fact that chaser spacecraft evolving in the complex center subspace remain in bounded relative motion.[6] Using this parameterization, first-order approximations for quasiperiodic motion predict extrema in separation distance between the target and the chaser throughout a trajectory. Additionally, local toroidal coordinates are available as the state variables for a control scheme that maintains a desired relative trajectory.[7] Henry and Scheeres introduce the method of expansion maps, that explicitly use the quasiperiodic tori in the vicinity of periodic orbits to characterize the relative motion, and then predict extrema in relative distance and speed, as well as the phases at which those extrema occur along the torus.[8]

While useful for describing and designing quasiperiodic relative trajectories, the representations provided by local toroidal coordinates and expansion maps do not aid in characterizing non-quasiperiodic relative motion.

*Ph.D. Student, School of Aeronautics and Astronautics, Purdue University, West Lafayette, IN 47907; doming18@purdue.edu
†Hsu Lo Distinguished Professor of Aeronautics and Astronautics, School of Aeronautics and Astronautics, Purdue University, West Lafayette, IN 47907; howell@purdue.edu

In a more general treatment of the relative motion in the vicinity of periodic orbits, Burnett and Schaub represent the relative dynamics in terms of the modal decomposition of the relative states.[9] The challenge in this representation is a relative state no longer defined in terms of Cartesian coordinates; modal coordinates offer little physical intuition concerning the relative state. However, using this parameterization, the values of the modal state variables do yield insight into the evolution of the relative state over time, irrespective of the type of chaser relative trajectory. The modal decomposition also delivers a convenient set of state variables for targeting both relative trajectories and rendezvous.[9] This investigation relies on the modal decomposition as a means of designing passive loitering trajectories.

Another line of effort that appears in the literature for formation flying in multibody environments is loosely regarded as initialization into passively bounded relative motion. Barden focuses on a concept for periodic formation configurations that places chasers in the complex center manifold of an underlying periodic orbit, as applied in the Circular Restricted Three Body Problem (CR3BP),[10] and transitions the result into a higher-fidelity ephemeris model.[11] Howell and Marchand expand on this concept, using Floquet mode control to insert chaser spacecraft onto natural trajectories lying within the stable and center manifolds of a periodic orbit.[12] Relative motion on a selection of quasiperiodic orbits (QPOs) within the same family is also available, with attempts to parameterize the motion using longitudinal and latitudinal torus angles.[13] Also, recall the concept of expansion maps introduced by Henry and Scheeres[8] that are leveraged to design and understand spacecraft formations placed on QPOs. Strategies are also explored to place formations in regions of low or zero relative acceleration.[14,15] In contrast to formations explicitly placed within the center manifold, however, formations initialized in low relative acceleration regions require formation-keeping costs, even within the CR3BP.[16] Thus, differential corrections schemes are employed to target periodic relative orbits that return to the same relative state after a specified time interval,[17] but are not guaranteed to continue as periodic beyond the first return to the initial relative state. Natural loitering trajectories and forced relative trajectories through waypoints are also demonstrated.[18] Finally, Sandel and Sood investigate the use of optimal control to impact loitering and relative circumnavigation trajectories with and without explicit use of the periodic and quasiperiodic manifolds.[19]

In this investigation, the loitering trajectory design methodology is based on the knowledge that states lying within the center manifold associated with a generic periodic solution are guaranteed to exhibit bounded motion relative to the reference. While much of the research on relative motion within multibody environments is focused on placing relative orbits on QPOs, such is only one available option for periodic orbits that possess a complex center manifold. However, center manifolds for periodic orbits in the CR3BP generally include trajectories positioned at different phases along the reference orbit (analogous to a String of Pearls Formation, or SPF) or on Nearby Periodic Orbits (NPOs). With SPF and NPO modes identified as possible options for long-term loitering in the vicinity of any CR3BP orbit, as well as the potential presence of QPO modes, this investigation then leverages the modal decomposition of the State Transition Matrix (STM) to predict general features of such behavior within each of the modes in the center subspace. From the propagation of modal states, the boundaries for the set of allowable loitering trajectories, i.e., trajectories that remain within the minimum and maximum acceptable separation distances, are produced. Rendezvous maneuvers are then constructed from the final states along the loitering trajectories and the combined solution space for the loitering and rendezvous phases is characterized. Finally, loitering trajectories that lead to minimum-cost rendezvous maneuvers are targeted by leveraging modal coordinates in a locally optimal differential corrections scheme.

DYNAMICAL BACKGROUND

In this investigation, the CR3BP is employed as the model to characterize the dynamics that govern spacecraft behavior. Within the formulation of the CR3BP, two primary bodies, in this case the Earth (P_1) and the Moon (P_2), orbit their mutual barycenter (B) in Keplerian circular orbits. The motion of the two primaries is labeled the primary system. A third body (P_3) represents the spacecraft, and it is assumed that the spacecraft has negligible mass relative to the primaries. Thus, the spacecraft does not affect the motion of the primary system. The dynamics of the CR3BP are formulated in a reference frame, $\mathcal{S} = \{\hat{x}_s, \hat{y}_s, \hat{z}_s\}$, known as the barycentric synodic frame, that is centered at the barycenter and rotates with the primary system, as illustrated

in Figure 1(a). The unit vector $\hat{x}_s$ is directed from the barycenter towards P_2, $\hat{z}_s$ is aligned with the angular momentum direction of the primary system, and $\hat{y}_s$ completes the orthonormal triad. The second-order scalar equations of motion of the spacecraft as formulated in the barycentric synodic frame are

$$\ddot{x} = 2\dot{y} + \frac{\partial U^*}{\partial x}, \qquad \ddot{y} = -2\dot{x} + \frac{\partial U^*}{\partial y}, \qquad \ddot{z} = \frac{\partial U^*}{\partial z} \tag{1}$$

where U^* is a pseudo-potential function dependent only on the position of the spacecraft. The CR3BP possesses one scalar integral of the motion, known as the Jacobi constant, that is dependent on the position of the spacecraft and the magnitude of the spacecraft velocity in the barycentric synodic frame, and is defined as

$$\mathcal{C} = 2U^* - (\dot{x}^2 + \dot{y}^2 + \dot{z}^2) \tag{2}$$

The presence of $\mathcal{C}$ indicates that periodic orbits in the CR3BP exist in families, with adjacent periodic orbits occurring at different values of the Jacobi constant.

When examining relative motion, it is also advantageous to define the relative synodic reference frame, $\mathcal{T} = \{\hat{x}, \hat{y}, \hat{z}\}$, centered at the hub, with basis unit vectors aligned with their barycentric synodic frame counterparts. The vector and frame definitions associated with relative motion appear in Figure 1(b). While other relative frames are available, e.g., the LVLH frame,[18,19] the relative synodic frame aids analysis by capturing the relative motion without introducing additional assumptions or basis vector rotations.

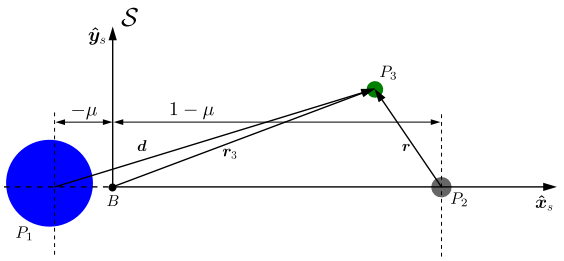

(a) CR3BP Schematic

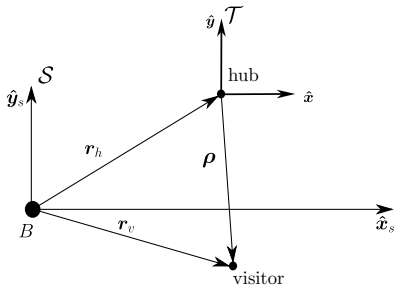

(b) Relative position and definition of the relative synodic frame $\mathcal{T}$.

Figure 1: Vector and Frame Definitions

Periodic Orbits

Knowledge of the stability of the periodic solutions within the CR3BP is a focus for designing long-duration ballistic loitering trajectories. The stability of a periodic solution in a dynamical model is assessed from the eigenvalues (λ_i) of the full-period State Transition Matrix (STM), i.e., the monodromy matrix (M). Eigenvalues with magnitudes greater than, equal to, and less than 1 indicate unstable, center, and stable modes, respectively. Because of the autonomous and symplectic nature of the CR3BP equations of motion, the eigenvalues of M must occur in three reciprocal pairs, with one pair, known as the trivial pair, guaranteed to be equal to one. A consequence of the reciprocal pairing of eigenvalues is that all stable eigenvalues are paired with unstable ones, forming saddle modes, implying that linearly stable periodic orbits within the CR3BP do not exist. Only marginally stable and unstable periodic orbits are available.

The center subspace for a periodic orbit is spanned by eigenvectors corresponding to eigenvalues with unit magnitude. Two subspaces within the center subspace are further defined: the trivial subspace and the complex center subspace. The trivial subspace is spanned by the eigenvectors associated with the trivial pair of eigenvalues. However, the trivial eigenvalues are, in general, defective; the algebraic multiplicity is two while the geometric multiplicity is only one. Thus, the basis of the trivial subspace comprises an ordinary eigenvector, directed along the periodic orbit, and a generalized eigenvector, directed towards neighboring periodic orbits along the family that exist at different values of the Jacobi constant. While the trivial subspace is

defined for CR3BP periodic orbits in general, as the monodromy matrix is guaranteed to possess the trivial pair of eigenvalues, the complex center subspace is only defined for a periodic orbit if the monodromy matrix has complex eigenvalues that lie on the unit circle. The eigenvectors associated with the complex unit magnitude eigenvalues span the complex center subspace. The trivial subspace linearly approximates the portion of the center manifold that consists of nearby periodic trajectories, while the complex center subspace linearly approximates nearby quasiperiodic motion. By leveraging linear approximations, preliminary design of relative trajectories is accomplished without the additional complexity of constructing periodic and quasiperiodic orbits in the full nonlinear model.

The eigendecomposition of the monodromy matrix is leveraged to construct the STM for a periodic solution explicitly as a function of its stability modes. Per the Floquet-Lyapunov Theorem,[20,21] the STM is decomposed into the form

$$\phi(t, t_0) = F(t)e^{J(t-t_0)}F^{-1}(t_0) \tag{3}$$

where $F(t)$ is a periodic matrix with period equal to that of the reference periodic orbit, and J is a block diagonal matrix. The columns of F are the Floquet modes, and F is defined as

$$F(t) = \begin{bmatrix} \boldsymbol{f}_1(t) & \boldsymbol{f}_2(t) & \boldsymbol{f}_3(t) & \boldsymbol{f}_4(t) & \boldsymbol{f}_\Gamma(t) & \boldsymbol{f}_f(t) \end{bmatrix} \tag{4}$$

where the values of each $\boldsymbol{f}_i$ at the initial time are equivalent to the eigenvectors of the monodromy matrix. Recall that the eigenvectors corresponding to the trivial pair of eigenvalues are directed along the orbit and tangent to the family. Thus, of particular importance, $\boldsymbol{f}_\Gamma$ and $\boldsymbol{f}_f$ represent the Floquet modes that are oriented in the phase velocity and family directions. The numbered Floquet modes $\boldsymbol{f}_i$ correspond to complex center or saddle motion, depending on the stability properties of the reference periodic orbit. Assuming the existence of a complex center subspace, the corresponding Floquet modes are labeled $\boldsymbol{f}_{ci}$. The variational state $\delta\boldsymbol{x}$ is expressed in modal coordinates $\boldsymbol{\alpha}$ as

$$\delta\boldsymbol{x}(t) = F(t)\boldsymbol{\alpha}(t) \tag{5}$$

where the modal coordinates are functions of time such that

$$\boldsymbol{\alpha}(t) = e^{J(t-t_0)}\boldsymbol{\alpha}(t_0) \tag{6}$$

and the initial conditions are expressed as

$$\boldsymbol{\alpha}(t_0) = F^{-1}(t_0)\delta\boldsymbol{x}(t_0) = \begin{bmatrix} \alpha_{1,0} & \alpha_{2,0} & \alpha_{3,0} & \alpha_{4,0} & \alpha_{\Gamma,0} & \alpha_{f,0} \end{bmatrix}^T \tag{7}$$

Each $\alpha_{i,0}$ term in Equation (7) corresponds to the Floquet modes in Equation (4). The variational state, expressed as a function of time and with an initial condition expressed in modal coordinates, is thus written as

$$\delta\boldsymbol{x}(t) = F(t)e^{J(t-t_0)}\boldsymbol{\alpha}(t_0) \tag{8}$$

For the purposes of designing loitering orbits, the Floquet decomposition offers some distinct advantages over the direct use of the STM for linear analysis. Since the Floquet matrix is periodic, the maximum time that the STM must be propagated to produce the Floquet matrix is precisely one period, thus, reducing the numerical error associated with long numerical propagations. Additionally, the ability to utilize the Floquet coefficients to directly select and propagate states within the various modes of the center subspace is leveraged extensively in this investigation.

While all of the eigenvalues equally describe the stability characteristics of a periodic orbit, it is advantageous to quantify the divergence associated with the most unstable mode as a single value. As such, the stability of a periodic orbit is represented using a quantity termed the maximum stability index,

$$\nu = \|\boldsymbol{\lambda}\|_\infty \tag{9}$$

where $\|\boldsymbol{\lambda}\|_\infty$ denotes the infinity norm of the vector of eigenvalues for M. Thus, the maximum stability index ν is the magnitude of the largest eigenvalue for M. After each revolution, relative states in the most unstable direction grow by a factor of ν. The maximum stability index is coupled with the period of the periodic orbit,

however, making stability comparisons between orbits of different periods difficult. Thus, a related term, known as the time constant, is defined as

$$\tau = \frac{\mathbb{P}}{\ln \nu} \tag{10}$$

where $\mathbb{P}$ denotes the period of the orbit. The time constant is the time required for unstable divergence to grow by a factor of e. As ν approaches 1, i.e., as an underlying periodic orbit becomes closer to linearly stable, the time constant τ approaches infinity.

Within this investigation, three periodic orbits are leveraged as sample hub orbits, plotted in Figure 2. These orbits, the 2:1 synodic resonant southern L_2 halo orbit, a Distant Retrograde Orbit (DRO), and an L_1 Lyapunov orbit, represent a range of geometries, locations within cislunar space, and stability properties. Table 1 summarizes relevant information for each of the sample orbits. Note that the stability information in the table excludes the trivial subspace, and the label "center" refers to the complex center subspace. The L_2 halo orbit and the L_1 Lyapunov orbit are both linearly unstable orbits with time constants shorter than 3 days. The L_1 Lyapunov orbit possesses two saddle modes while the L_2 halo orbit, though linearly unstable, does possess a complex center subspace. Meanwhile, the time constant for the linearly marginally stable DRO is infinity, and the complex center subspace for the DRO contains pairs of in-plane and out-of-plane eigenvectors.

Table 1: **Parameters for Sample Hub Orbits**

Orbit	Geometry	Stability	$\mathbb{P}$ (days)	ν	τ (days)
L_2 halo	Spatial	saddle $\times$ center	14.77	1010.7	2.13
L_1 Lyapunov	Planar	saddle $\times$ saddle	17.09	408.7	2.84
DRO	Planar	center $\times$ center	5.77	1	∞

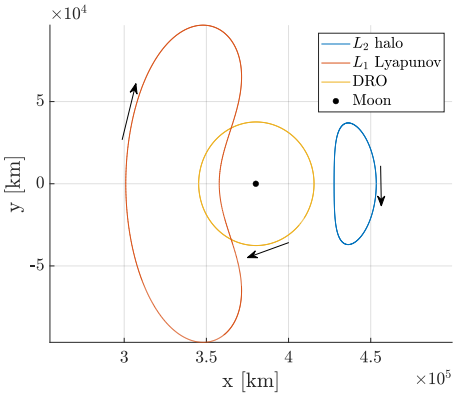

Figure 2: Sample hub orbits

Quasiperiodic Orbits

Quasiperiodic trajectories exist on higher-dimensional tori that are associated with an underlying periodic orbit. Thus, the trajectories remain bounded within the vicinity of the periodic orbit but never return precisely to their initial states, as they are not generally periodic. While a single state along a periodic orbit, propagated infinitely, remains on the closed curve of the same periodic orbit, an infinitely long quasiperiodic trajectory fills out the toroidal surface in phase space. Similarly, the stroboscopic map constructed by sampling an infinitely long quasiperiodic trajectory after every period of the underlying periodic orbit is a solid and closed curve termed the invariant curve. The stroboscopic map constructed from an infinitely long periodic trajectory

simply returns the initial state as a fixed point. Consecutive returns to the stroboscopic map are, within the linearized dynamics, rotated by a rotation angle $\phi_L = \arg \lambda_Q$, where λ_Q is the complex eigenvalue of the monodromy matrix for the underlying periodic orbit. As quasiperiodic trajectories return to the invariant curve after each stroboscopic period, the invariant curve is itself a periodic structure.

The linear approximation for an invariant curve associated with a given fixed point along a periodic orbit is constructed by perturbing the fixed point state into the complex center subspace. Although the complex center subspace is defined by complex eigenvectors $\boldsymbol{v}_{ci}$ corresponding to the complex eigenvalues, the real and imaginary parts of a single complex eigenvector $\boldsymbol{v}_{c1}$ span the complex center subspace. The invariant curve is, thus, approximated by

$$\delta \boldsymbol{x}_c = \epsilon \frac{\mathrm{Re}\left[\boldsymbol{v}_{c1}\right] \cos\theta - \mathrm{Im}\left[\boldsymbol{v}_{c1}\right] \sin\theta}{\kappa} \tag{11}$$

where ϵ is the step-off distance into the center subspace and κ is a scaling factor that is typically equivalent to the magnitude of the position component of the complex eigenvector. Quasiperiodic orbits are targeted in the full nonlinear dynamics such that every nonlinearly propagated state on the invariant curve rotates by the same angle ϕ after each mapping period.[22–24] Nonlinear QPOs are then continued in families defined by a fixed value of one of three parameters: Jacobi constant, rotation angle, or mapping time.[24] The remaining two parameters are permitted to vary throughout the continuation process. The choice of fixed parameter results in families that exhibit different characteristics and are suitable for different applications. For example, families of nonlinear QPOs constructed by fixing Jacobi constant are advantageous for applications such as transfers that require spacecraft at a particular energy level. As long-term ballistic loitering behavior is desired for this investigation, however, only constant stroboscopic mapping time nonlinear QPOs are evaluated, where the stroboscopic period is equal to the period of the underlying periodic orbit.

Differential Corrections

A differential corrections scheme is implemented leveraging a free variable-constraint formulation to target solutions for the loitering and rendezvous problems. The targeting method defines an $n \times 1$ free variable vector and an $m \times 1$ constraint vector as $\boldsymbol{X} = [X_1, \ldots, X_n]^T$ and $\boldsymbol{F}(\boldsymbol{X}) = [F_1(\boldsymbol{X}), \ldots, F_m(\boldsymbol{X})]^T$, where the superscript T implies transpose. The $m \times n$ Jacobian matrix $DF(\boldsymbol{X}) = \partial \boldsymbol{F} / \partial \boldsymbol{X}$ is employed to update the free variables iteratively until the constraint vector is driven to zero, within a numerical tolerance. If $m = n$, then the inverse of $DF(\boldsymbol{X})$ exists, and the problem is considered square. The free variable vector is updated with

$$\boldsymbol{X}_i = \boldsymbol{X}_{i-1} - DF(\boldsymbol{X}_{i-1})^{-1} \boldsymbol{F}(\boldsymbol{X}_{i-1}) \tag{12}$$

Analytically or numerically constructed partial derivatives are employed in the DF matrix. All targeting problems in this investigation are square.

Once the differential corrections algorithm converges to a single point solution, nearby solutions are constructed by leveraging Pseudo-ArcLength Continuation (PALC). Assume an underconstrained targeting scheme with n free variables and $m = n - 1$ constraints contained in $\boldsymbol{X}_c$ and $\boldsymbol{F}_c$, with an associated $(n-1) \times (n)$ Jacobian matrix DF_c . An additional constraint is added to the targeting problem, such that

$$\boldsymbol{X}_d = \boldsymbol{X}_c, \qquad \boldsymbol{F}(\boldsymbol{X}) = \begin{bmatrix} \boldsymbol{F}_c \\ F_{palc} \end{bmatrix} = \begin{bmatrix} \boldsymbol{F}_c \\ \left(\boldsymbol{X}_{\boldsymbol{i}} - \boldsymbol{X}^*_{i-1}\right)^T \mathcal{N}_{i-1} - \delta s \end{bmatrix} = \boldsymbol{0} \tag{13}$$

where $\boldsymbol{X}^*_{i-1}$ is the previously converged free variable vector and δs is a user-provided step size. The $n \times 1$ vector $\mathcal{N}_{i-1}$ represents the one-dimensional nullspace of DF_c, that is the Jacobian of $\boldsymbol{F}_c$ with respect to $\boldsymbol{X}^*_{i-1}$. The targeter used for PALC is a square problem, with n free variables and $m = n$ constraints.

NATURAL RELATIVE MOTION

The basic loitering scenario employed in this investigation introduces two types of spacecraft: the hub and the visitor. The hub spacecraft is in a predetermined, permanent cislunar orbit with period $\mathbb{P}$, although the methodology examined within this investigation applies to any multibody environment where the CR3BP is a

reasonable dynamical model. The visitor spacecraft is arriving in the vicinity of the hub, but must be placed into a loitering orbit to accommodate the physical and scheduling limitations at the hub before it initiates a rendezvous and dock operation.

Long-duration ballistic loitering trajectories in the vicinity of the hub are placed in the center subspace for the hub orbit, since the unstable modes for the relative visitor motion otherwise dominate, leading to relative divergence of the two spacecraft. Figure 3 demonstrates relative motion on unstable, quasiperiodic, and periodic trajectories in the vicinity of a hub in the L_2 halo orbit. Visitors on unstable trajectories exponentially diverge from the hub motion, whereas visitors on quasiperiodic trajectories oscillate about their initial conditions without any long-term growth. Nearby periodic trajectories offer two types of behavior: String of Pearls Formation (SPF) motion that is perfectly periodic in the barycentric synodic and relative frames, and Nearby Periodic Orbit (NPO) motion where the visitor gradually drifts out of phase with the hub. Throughout this investigation, analysis of the linear center *subspace* serves as a tool to inform design of nonlinear trajectories within the center *manifold*. In this section, the Floquet decomposition of the linear variational state is leveraged to gain insights into periodic and quasiperiodic relative motion in the center subspace.

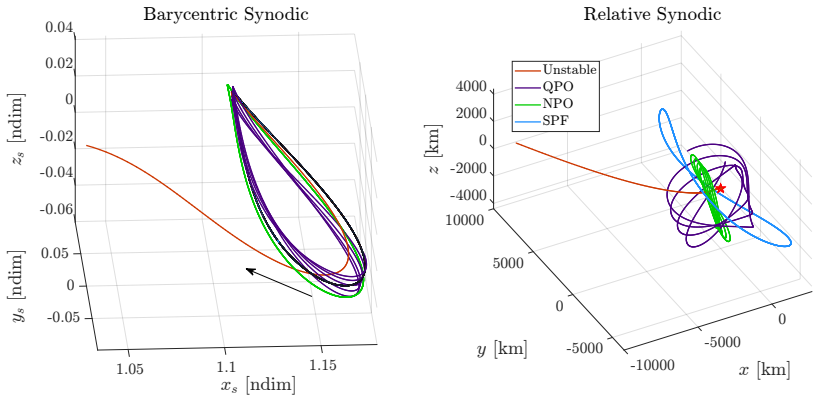

Figure 3: Relative Motion About the L_2 Halo Orbit

Relative Motion on Nearby Periodic Trajectories

The design of loitering orbits by exploiting nearby periodic trajectories is accomplished using the Floquet decomposition of linear variational states. The Floquet decomposition is leveraged because undesirable modes of motion, such as stable and unstable behavior, are explicitly excluded through manipulation of the Floquet coefficients. Employing Equations (7) and (8) and setting $\alpha_{1,0}$ through $\alpha_{4,0}$ equal to zero, the linear approximation for a state lying within the trivial subspace of the hub orbit, i.e., a state lying on a periodic orbit in the vicinity of the hub orbit, is

$$\delta \boldsymbol{x}(t) = \alpha_{\Gamma,0} \boldsymbol{f}_\Gamma(t) + \alpha_{f,0} \frac{t}{\mathbb{P}} \boldsymbol{f}_\Gamma(t) + \alpha_{f,0} \boldsymbol{f}_f(t) \tag{14}$$

where $\boldsymbol{f}_\Gamma$ and $\boldsymbol{f}_f$ are defined in Equation (4). The initial relative state is expressed using only the Floquet coefficients $\alpha_{\Gamma,0}$ and $\alpha_{f,0}$. Positive and negative values for $\alpha_{\Gamma,0}$ correspond to relative states ahead of and behind the hub in the phase velocity direction, whereas positive and negative values of $\alpha_{f,0}$ correspond to relative states on NPOs with shorter and longer periods than the hub. Nearby periodic orbits with shorter periods than the hub are labeled "faster" orbits while NPOs with longer periods than the hub are labeled "slower" orbits. By leveraging the Floquet decomposition, linear approximations of trajectories along nearby faster and slower orbits are evaluated for loitering without explicitly targeting such orbits in the full nonlinear model.

In the general case where $\alpha_{f,0} \neq 0$, secular drift arising from the generalized eigenvector in the monodromy matrix is readily apparent, as the $\alpha_{f,0} \frac{t}{\mathbb{P}}$ term in Equation (14) forces the phase of the visitor to drift along the phase velocity direction $\boldsymbol{f}_\Gamma$ over time. A schematic illustrating $\boldsymbol{f}_\Gamma$ and $\boldsymbol{f}_f$ in the context of relative motion

on a nearby faster orbit is displayed in Figure 4. A visitor, marked in red, is initialized along $\boldsymbol{f}_f$ such that $\alpha_{\Gamma,0} = 0$ and $\alpha_{f,0} = 1$. The state of the visitor after one period $\mathbb{P}$ of the hub orbit appears in blue, and the hub location, marked in black, remains the same at both times. At $t = \mathbb{P}$, the relative state of the hub becomes $\boldsymbol{f}_\Gamma + \boldsymbol{f}_f$ to reflect the drift that has occurred in the phase velocity, i.e., $\boldsymbol{f}_\Gamma$, direction. After k hub orbits, the component of the relative state along the phase velocity direction increases by $k\alpha_{f,0}\boldsymbol{f}_\Gamma$ while the along family component of the relative state remains equal to $\alpha_{f,0}\boldsymbol{f}_f$. Since the relative magnitudes of $\boldsymbol{f}_f$ and $\boldsymbol{f}_\Gamma$ are determined from solving the generalized eigenvector problem for a particular monodromy matrix, different orbits exhibit different amounts of phase drift. To quantify this behavior, a phase drift metric is defined as

$$\xi_t = \frac{1}{\mathbb{P}} \frac{\|\boldsymbol{f}_{\Gamma,r}\|}{\|\boldsymbol{f}_{f,r}\|} \tag{15}$$

where $\boldsymbol{f}_{\Gamma,r}$ and $\boldsymbol{f}_{f,r}$ are the position components of $\boldsymbol{f}_\Gamma$ and $\boldsymbol{f}_f$, respectively. The division of $\|\boldsymbol{f}_{\Gamma,r}\|$ by $\|\boldsymbol{f}_{f,r}\|$ represents the ratio, after one hub revolution, of position-space drift in the phase velocity direction to the initial along family component of the relative state. The ratio is divided by $\mathbb{P}$ to allow for comparison of phase drift between orbits with differing periods. While the specific value of ξ_t is dependent on the location at which it is calculated along the periodic orbit, it is nonetheless an indicator of the rate at which nearby periodic orbits drift out of phase. The NPO motion exhibited by the L_2 halo ($\xi_t = 0.041$), L_1 Lyapunov ($\xi_t = 5.25$), and DRO ($\xi_t = 7.04$) appears in Figure 5. In each plot, separation distances are normalized by their initial values. The L_2 halo has a significantly smaller value of ξ_t than the other two orbits, and as such the normalized separation distance grows by two orders of magnitude less than for the other orbits in a linear approximation.

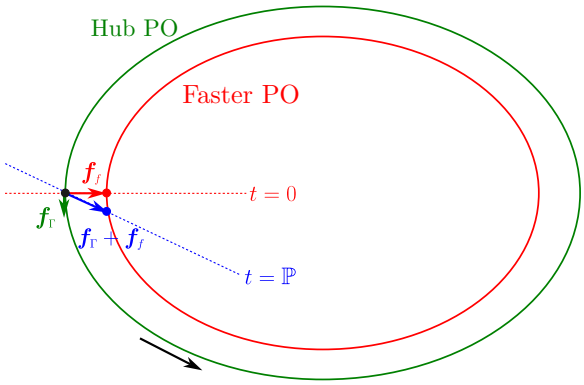

Figure 4: Schematic of Phase Drift ($\alpha_{\Gamma,0} = 0, \alpha_{f,0} = 1$)

Relative Motion on Nearby Quasiperiodic Trajectories

Similar to nearby periodic trajectories, the linear variational state for nearby quasiperiodic trajectories is expressed by leveraging the Floquet decomposition. Assuming that the hub orbit possesses multiple quasiperiodic modes via the complex center eigenvalues, then each one is considered separately. The numbered Floquet modes and modal coordinates in Equations (4) and (7) are renamed to specifically refer to the complex center subspace, such that the quasiperiodic variational state is expressed using only two Floquet vectors, $\boldsymbol{f}_{c1}$ and $\boldsymbol{f}_{c2}$, as in

$$\delta\boldsymbol{x}(t) = [\alpha_{c1,0}\cos\theta_c t + \alpha_{c2,0}\sin\theta_c t]\,\boldsymbol{f}_{c1}(t) + [-\alpha_{c1,0}\sin\theta_c t + \alpha_{c2,0}\cos\theta_c t]\,\boldsymbol{f}_{c2}(t) \tag{16}$$

where $\alpha_{c1,0}$ and $\alpha_{c2,0}$ represent the initial Floquet coefficients and θ_c denotes the complex part of the Poincaré exponent associated with the complex center eigenvalues of the monodromy matrix. In contrast to relative motion in the trivial subspace, there is no secular growth along a particular axis; instead, the relative motion is characterized by oscillatory behavior such that relative motion of the visiting spacecraft rotates by a latitudinal angle over time. This behavior is captured in the sinusoidal terms of Equation (16), where the angle θ_c is the rotation frequency.

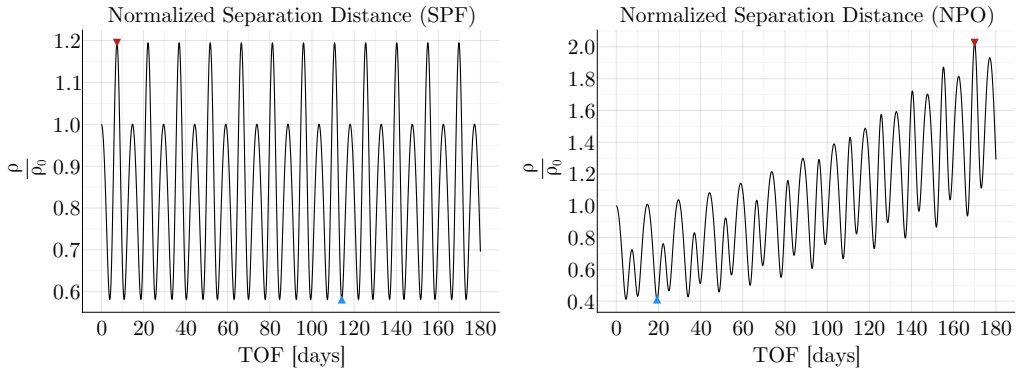

(a) 2:1 synodic resonant L_2 halo ($\mathbb{P} = 14.8$ days, $\xi_t = 0.041$)

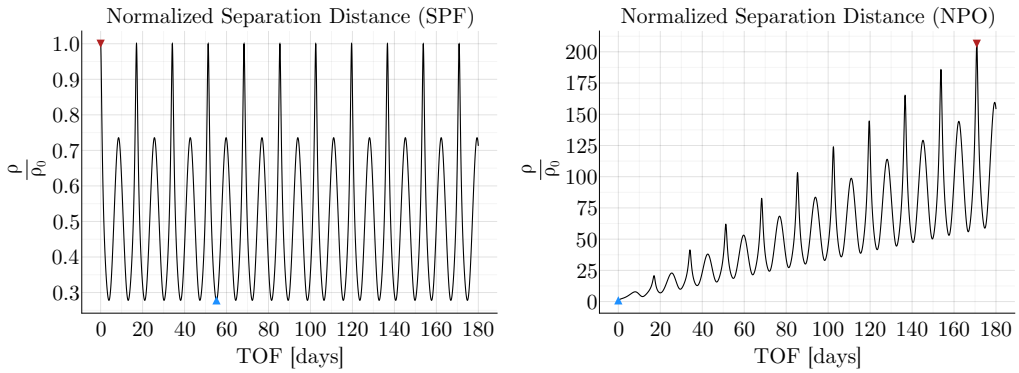

(b) L_1 Lyapunov ($\mathbb{P} = 17.1$ days, $\xi_t = 5.25$)

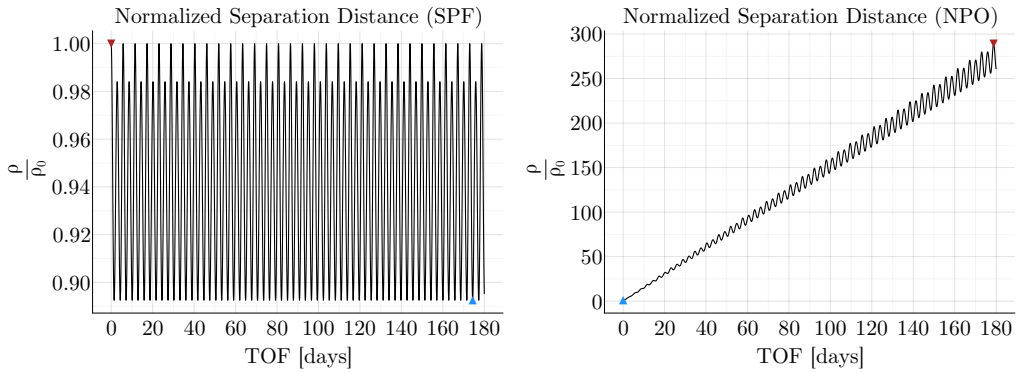

(c) DRO ($\mathbb{P} = 5.77$ days, $\xi_t = 7.04$)

Figure 5: The evolution is demonstrated, over a 180-day propagation time, for separation distance over time from the linear propagation of SPF and NPO trajectories in the vicinity of sample hub orbits.

By leveraging a strategy analogous to Elliott and Bosanac, the change in size, shape, and orientation of the QPO invariant curve over one period are predicted by applying the singular value decomposition (SVD) to the Floquet modal vectors governing the complex center subspace.[6] Thus, the Floquet modes are decomposed as

$$F_{c,r} = \begin{bmatrix} \boldsymbol{f}_{c1,r} & \boldsymbol{f}_{c2,r} \end{bmatrix} = U \Sigma V^T \tag{17}$$

where U and Σ contain the directions and magnitudes of the semimajor and semiminor axes of the invariant curve, respectively, and V is the rotation matrix between U and $F_{c,r}$. The lengths of the semimajor and semiminor axes, constructed over exactly one period of the hub orbit and normalized by the initial value of the semimajor axis, provide the minimum and maximum expected growth of QPO states as a function of time. Since the invariant curve is periodic, it is not necessary to propagate for longer than a single hub period. Figure 6 demonstrates the separation envelope that bounds linearly propagated QPO trajectories for the L_2 halo orbit and the DRO. For example, in the case of the L_2 halo, any visitor initialized on a QPO torus with semimajor axis a_0 at the initial time has a separation distance bounded between approximately $0.4a_0$ and $1.1a_0$ for all time.

For many planar orbits, the complex center subspace exists entirely out-of-plane, i.e., the complex center eigenvectors only have z and $\dot{z}$ components, resulting in one of the vectors $\boldsymbol{f}_{c1,r}$ or $\boldsymbol{f}_{c2,r}$ equal to a zero vector. Indeed, one of the two complex center modes for the DRO hub orbit exhibits this geometry. In such cases, the SVD analysis in Equation (17) demonstrates that the invariant curve is reduced from an ellipse to a line, that is, the minimum separation distance is zero. For loitering purposes, it is not acceptable for the visitor spacecraft to collide with the hub spacecraft. Therefore, such QPOs are not suitable for loitering and are excluded from consideration.

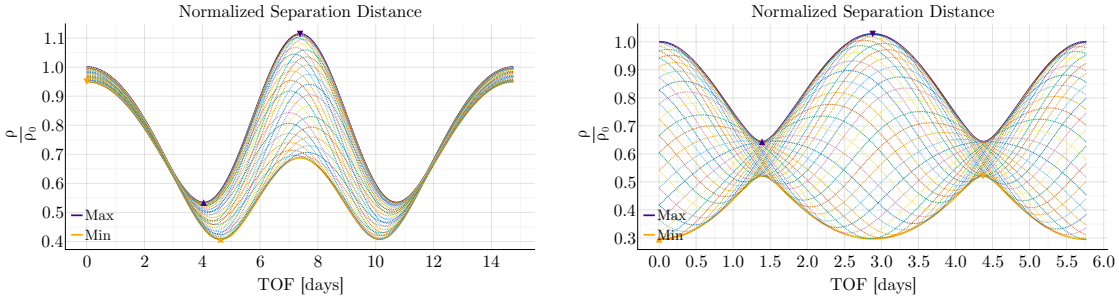

(a) 2:1 synodic resonant L_2 halo ($\mathbb{P} = 14.8$ days)

(b) DRO ($\mathbb{P} = 5.77$ days)

Figure 6: Predicted Separation Envelopes for QPOs

DESIGN OF LOITERING TRAJECTORIES

The design of loitering trajectories leverages the linear variational equations for relative motion within the center subspace. It is assumed that the time duration for the loitering phase, denoted T_L, is known *a priori*. Additionally, parameters ρ_{min} and ρ_{max} denote the minimum and maximum separation distances between the hub and the visitor throughout the duration of the loitering phase. Loitering options are determined via the eigenvalues of the monodromy matrix for the hub orbit. In some cases, the hub orbit lacks suitable complex eigenvalues, restricting the loitering options to SPF and NPO motion. However, since the subspaces containing nearby periodic and quasiperiodic trajectories are independent, loitering trajectory design associated with these eigenvector directions is approached separately. The set of initial conditions that satisfy the loitering parameters T_L, ρ_{min}, and ρ_{max} is, therefore, determined for each subspace.

The space of initial conditions that satisfies the loitering requirements, denoted $\mathcal{A}$, is the set of initial conditions that, when propagated for T_L, remain within the separation envelope defined by ρ_{min} and ρ_{max}. For loitering in the complex center subspace, initial conditions are parameterized by $\alpha_{c1,0}$ and $\alpha_{c2,0}$, whereas for loitering in the trivial subspace, initial conditions are parameterized by $\alpha_{\Gamma,0}$ and $\alpha_{f,0}$. The set $\mathcal{A}$ is bounded

by $\mathcal{A}_{min}$ and $\mathcal{A}_{max}$, i.e., the sets of initial conditions that produce trajectories with minimum and maximum separation distances of ρ_{min} and ρ_{max}, respectively. The boundaries $\mathcal{A}_{min}$ and $\mathcal{A}_{max}$ are constructed by leveraging differential corrections and numerical continuation.

Loitering on Nearby Periodic Trajectories

The free variable-constraint formulation of the differential corrections process is employed to construct $\mathcal{A}_{min}$ and $\mathcal{A}_{max}$. Each boundary curve is constructed separately, such that points on $\mathcal{A}_{min}$ are only guaranteed to include compliant minima and points on $\mathcal{A}_{max}$ are only guaranteed to have compliant maxima. In this manner, closed curves are constructed that are adjustable to reflect changes in ρ_{min} and ρ_{max} later in the design process. As the strategies for constructing $\mathcal{A}_{min}$ and $\mathcal{A}_{max}$ are nearly identical, only the construction of $\mathcal{A}_{max}$ is discussed in detail. For the construction of $\mathcal{A}_{max}$ in the trivial subspace, a 2×2 targeting problem is solved, where the free variable vector is

$$\boldsymbol{X}_p = \begin{bmatrix} \alpha_{\Gamma,0} \\ \alpha_{f,0} \end{bmatrix} \tag{18}$$

and the constraint vector is

$$\boldsymbol{F}(\boldsymbol{X}_p) = \begin{bmatrix} F_{max} \\ F_{palc} \end{bmatrix} = \boldsymbol{0} \tag{19}$$

such that

$$F_{max}(\boldsymbol{X}_p) = \max \rho(t; \boldsymbol{X}_p) - \rho_{max} \tag{20}$$

and $\rho(t; \boldsymbol{X}_p)$ is the scalar separation distance expressed as a function of the Floquet modes as

$$\rho(t; \boldsymbol{X}_p) = \left[\left(\alpha_{\Gamma,0}^2 + 2\alpha_{\Gamma,0}\alpha_{f,0}\frac{t}{\mathbb{P}} + \alpha_{f,0}^2\frac{t^2}{\mathbb{P}^2} \right) \boldsymbol{f}_\Gamma^T N \boldsymbol{f}_\Gamma + \left(2\alpha_{\Gamma,0}\alpha_{f,0} + 2\alpha_{f,0}^2\frac{t}{\mathbb{P}} \right) \boldsymbol{f}_\Gamma^T N \boldsymbol{f}_f + \alpha_{f,0}^2 \boldsymbol{f}_f^T N \boldsymbol{f}_f \right]^{\frac{1}{2}} \tag{21}$$

The matrix N, originating from selecting just the position states, is a 6×6 matrix filled with zeros, with the exception of ones occupying the first three diagonal elements. The separation distance ρ is purely a function of time, as the Floquet coefficients $\alpha_{\Gamma,0}$ and $\alpha_{f,0}$ are constant parameters of the function that represents the initial relative state of the visitor spacecraft. The constraint F_{max} ensures that the minimum separation distance for the converged solution is equivalent to ρ_{max}, and the pseudo-arclength constraint F_{palc} is leveraged to continue the family of solutions. The free variable vector $\boldsymbol{X}_p$ is then iteratively updated, as in Equation (12), until the constraints are satisfied within a numerical tolerance.

Initial solutions to the targeting problem are based on the separation distance normalized by the initial value, $\frac{\rho}{\rho_0}$, evaluated over the loitering time period for $\alpha_{f,0} = 0$ (pure SPF). The maximum value of $\frac{\rho}{\rho_0}$ produces the initial separation distance in the $\boldsymbol{f}_\Gamma$ direction, $\rho_{\Gamma,0}$, that results in a maximum separation distance equal to ρ_{max}, as in

$$\rho_{\Gamma,0} = \frac{\rho_{max}}{\max \frac{\rho}{\rho_0}} \tag{22}$$

The same procedure is also executed for $\alpha_{\Gamma,0} = 0$ (pure NPO) to determine the initial separation distance along the $\boldsymbol{f}_f$ direction, i.e., $\rho_{f,0}$. Assuming a loitering time $T_L = 180$ days, the $\frac{\rho}{\rho_0}$ curves as a function of time for three hub orbits are plotted in Figure 5, where maximum values are marked with red triangles. All three hub orbits yield similar results for the pure SPF case, as the maximum $\frac{\rho}{\rho_0}$ is between 1 and 1.2 for each orbit. However, for the pure NPO case, the L_1 Lyapunov orbit and the DRO require initial separation distances that are two orders of magnitude smaller than those for the L_2 halo orbit, as predicted by the relative magnitudes of ξ_t for each orbit. The initial separation distances along each Floquet mode $\rho_{i,0}$ are then converted to Floquet modal coefficients by

$$\alpha_{\Gamma,0} = \frac{\rho_{\Gamma,0}}{\|\boldsymbol{f}_{\Gamma,r}\|}, \qquad \alpha_{f,0} = \frac{\rho_{f,0}}{\|\boldsymbol{f}_{f,r}\|} \tag{23}$$

The resulting sets of Floquet coefficients, $(\alpha_{\Gamma,0}, 0)$ and $(0, \alpha_{f,0})$, as well as their reflections across the origin, are points on $\mathcal{A}_{max}$ that are produced without iteration. These points are leveraged as the initial points from which the targeting and continuation algorithm constructs the remainder of the $\mathcal{A}_{max}$ curve.

The minimum boundary curve $\mathcal{A}_{min}$ is generated following a similar procedure, substituting $\min$ for $\max$ in Equations (19), (20), and (22). Once $\mathcal{A}_{min}$ and $\mathcal{A}_{max}$ are constructed, the set of allowable initial conditions $\mathcal{A}$ is produced, as visualized in Figure 7 for the L_2 halo orbit and the DRO. The desired separation envelope for each example is defined by $\rho_{min} = 100$ km and $\rho_{max} = 500$ km. The loitering time is 180 days for the halo orbit example and 14 days for the DRO example. In Figure 7, $\mathcal{A}_{min}$ is outlined in red and $\mathcal{A}_{max}$ is outlined in purple. The green shaded regions correspond to $\mathcal{A}$, i.e., the set of all initial conditions that lie exterior to $\mathcal{A}_{min}$ and interior to $\mathcal{A}_{max}$. Purple shading represents initial conditions that have maxima larger than ρ_{max}, and light red shading corresponds to points that have minima smaller than ρ_{min}. Some initial conditions, shaded in dark red, violate both of the boundaries set by ρ_{min} and ρ_{max}.

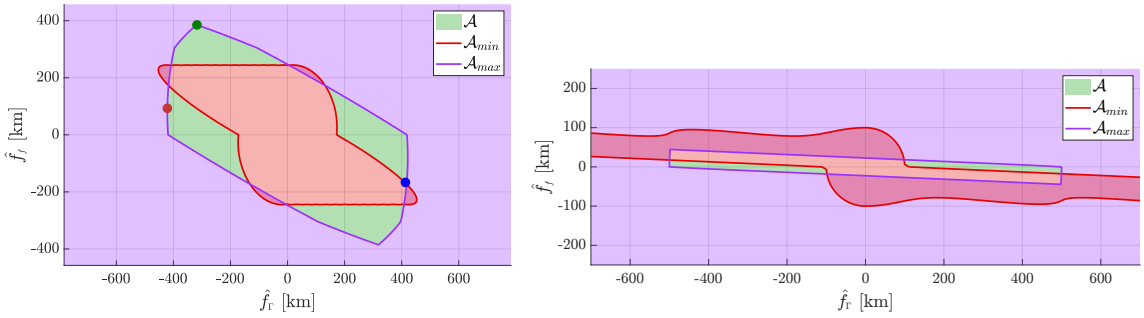

(a) L_2 halo, $T_L = 180$ days

(b) DRO, $T_L = 14$ days

Figure 7: Sets of Acceptable Initial Conditions (green) for $\rho_{min} = 100$ km and $\rho_{max} = 500$ km

Both examples demonstrate the effect of phase drift on loitering in the trivial subspace. Initial conditions indicated by the colored points in Figure 7(a) are propagated with the nonlinear CR3BP dynamics for the loitering duration, and the resulting relative trajectories, along-track phase, and separation distances are correspondingly plotted in Figure 8(a). The visitor on the red trajectory is initialized behind the hub on a faster periodic orbit, since it has negative $\alpha_{\Gamma,0}$ and positive $\alpha_{f,0}$ values. Secular drift along the red trajectory results in the visitor approaching the hub in along-track phase. Similarly, the blue trajectory is initialized ahead of the hub in a slower orbit ($\alpha_{\Gamma,0} > 0, \alpha_{f,0} < 0$), resulting in a similar separation distance history, where the visitor phase gradually falls back towards the hub. The green trajectory, similar to the red trajectory, is initialized behind the hub on a faster orbit. However, it is initialized much farther away, nearly at the edge of the separation envelope, and with $\alpha_{f,0}$ nearly 5 times greater than for the red trajectory. The green visitor overtakes the hub in the along-track direction during the loitering period but never approaches ρ_{min} in separation distance, since the periodic orbit for the green trajectory is sufficiently far from the hub orbit. In the case of the DRO, loitering trajectories with behavior analogous to the red and blue trajectories are available, since the $\mathcal{A}$ regions exist exterior to $\mathcal{A}_{min}$ in the upper right and bottom left sides of the plot in Figure 7(b). However, the region from which the green trajectory is sampled does not exist for the DRO for loitering time $T_L = 14$ days because the rate of phase drift, as predicted by ξ_t, is too high for loitering on periodic orbits sufficiently far away.

Loitering on Nearby Quasiperiodic Trajectories

Construction of the set of allowable initial conditions for quasiperiodic trajectories is achieved by adjusting the free variable vector and the constraints for the relative dynamics in the complex center subspace. The free variable vector becomes

$$\boldsymbol{X}_q = \begin{bmatrix} \alpha_{c1,0} \\ \alpha_{c2,0} \end{bmatrix} \tag{24}$$

and the constraint for $\mathcal{A}_{max}$ is analogous to Equation (20), where the separation distance ρ dependent on the value of $\boldsymbol{X}_q$ is

$$\rho(t; \boldsymbol{X}_q) = \left(a^2 \boldsymbol{f}_{c1}^T N \boldsymbol{f}_{c1} + 2ab \boldsymbol{f}_{c1}^T N \boldsymbol{f}_{c2} + b^2 \boldsymbol{f}_{c2}^T N \boldsymbol{f}_{c2}\right)^{\frac{1}{2}} \tag{25}$$

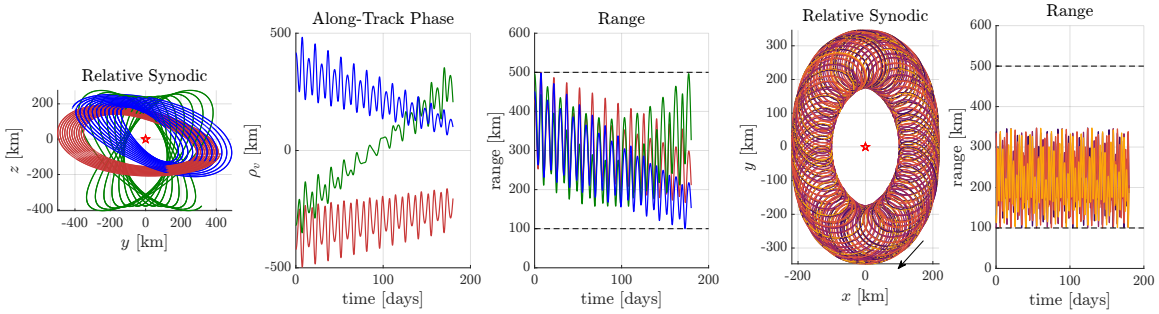

(a) NPO motion, L_2 halo, $T_L = 180$ days; colors correspond to initial condition points marked in Figure 7(a)

(b) Linear QPO motion from $\mathcal{A}_{min}$, DRO, $T_L = 180$ days; colors correspond to initial condition points marked in Figure 10(d)

Figure 8: Examples of Compliant Relative Motion

and

$$a(t; \boldsymbol{X}_q) = \alpha_{c1,0} \cos \theta_c t + \alpha_{c2,0} \sin \theta_c t \tag{26}$$

$$b(t; \boldsymbol{X}_q) = -\alpha_{c1,0} \sin \theta_c t + \alpha_{c2,0} \cos \theta_c t \tag{27}$$

Initial solutions to the targeting problem for loitering in the complex center subspace are also determined from $\frac{\rho}{\rho_0}$. The initial conditions $\boldsymbol{X}_q = [1, 0]$ and $\boldsymbol{X}_q = [0, 1]$ are propagated for T_L, minimum and maximum values of $\frac{\rho}{\rho_0}$ are produced, and the Floquet coefficients resulting in points on $\mathcal{A}_{min}$ and $\mathcal{A}_{max}$ are constructed by leveraging Equations (22) and (23). The plots for $\frac{\rho}{\rho_0}$ as a function of time for the L_2 halo orbit and the DRO appear in Figure 9 for $T_L = 180$ days. The lack of secular terms within Equation (25) results in separation distance being bounded. The shape of the invariant curve also affects the plots in Figure 9. The invariant curve for the DRO is much more eccentric than for the L_2 halo, with the semimajor and semiminor axes initially aligned with $\boldsymbol{f}_{c1}$ and $\boldsymbol{f}_{c2}$, respectively. Thus, the separation distance along $\boldsymbol{f}_{c1}$ tends to be smaller than its initial starting value, with the opposite being true for the state initialized along $\boldsymbol{f}_{c2}$. The targeting and continuation algorithm for computing $\mathcal{A}_{min}$ and $\mathcal{A}_{max}$ is then leveraged given the initial solutions that are constructed.

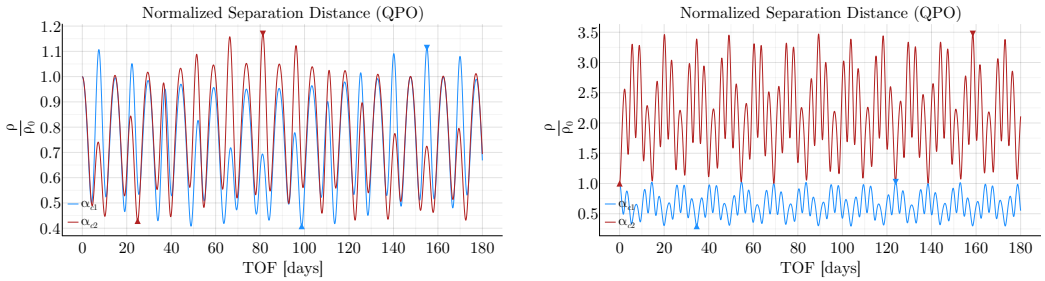

(a) L_2 halo

(b) DRO

Figure 9: Normalized separation distances for states initialized along $\boldsymbol{f}_{c1}$ and $\boldsymbol{f}_{c2}$

The allowable initial conditions for the L_2 halo orbit and the DRO are evolved for loitering times of 14 and 180 days, respectively, with the results appearing in Figure 10. The black lines in each plot represent sections of invariant curves with semimajor axes equal to 325 km at the initial time, projected onto the $\boldsymbol{f}_{c1} - \boldsymbol{f}_{c2}$ axes, that are compliant with the specified ρ_{min} and ρ_{max} boundaries. For all four examples, it is possible to construct a QPO such that all states on the torus are compliant. If the entire torus at the initial time is compliant

while $T_L < \mathbb{P}$, then it is possible to extend the loitering period for any state on the torus indefinitely without violating either ρ_{min} or ρ_{max}. The $\mathcal{A}_{min}$ and $\mathcal{A}_{max}$ curves tend to approximate the shape of the invariant curve as loitering time is increased to many multiples of $\mathbb{P}$. For shorter loitering times, however, there is an increased number of solutions within $\mathcal{A}$ that are compliant at specific phases without the entire torus itself being compliant. A partially compliant invariant curve is plotted in Figure 10(b), where the invariant curve contains points both interior and exterior to $\mathcal{A}_{min}$, depending on the phase. Selecting points from an invariant curve that is not entirely compliant can be advantageous, at the cost of limiting the potential for extending the loitering period indefinitely. For example, the partially compliant 325 km invariant curve for the DRO example in Figure 10(b) lies completely interior to the region enclosed by $\mathcal{A}_{min}$ if loitering time is increased to 180 days, such that no black curve is plotted in Figure 10(d).

Compliant trajectories propagated from the marked points along $\mathcal{A}_{min}$ in Figure 10(d) are plotted in Figure 8(b). The DRO possesses a planar complex center subspace, with $\boldsymbol{f}_{c1,r}$ aligned with the y axis and $\boldsymbol{f}_{c2,r}$ aligned with the x axis at the initial time. In contrast to the separation distance history for NPO motion, QPO motion remains bounded, with the separation distance bounded by the separation envelopes constructed in Figure 6(b). The design of a long-duration QPO loitering trajectory, when $\mathcal{A}_{min}$ and $\mathcal{A}_{max}$ more closely resemble the invariant curve, is generally reduced to selecting an acceptably-sized torus.

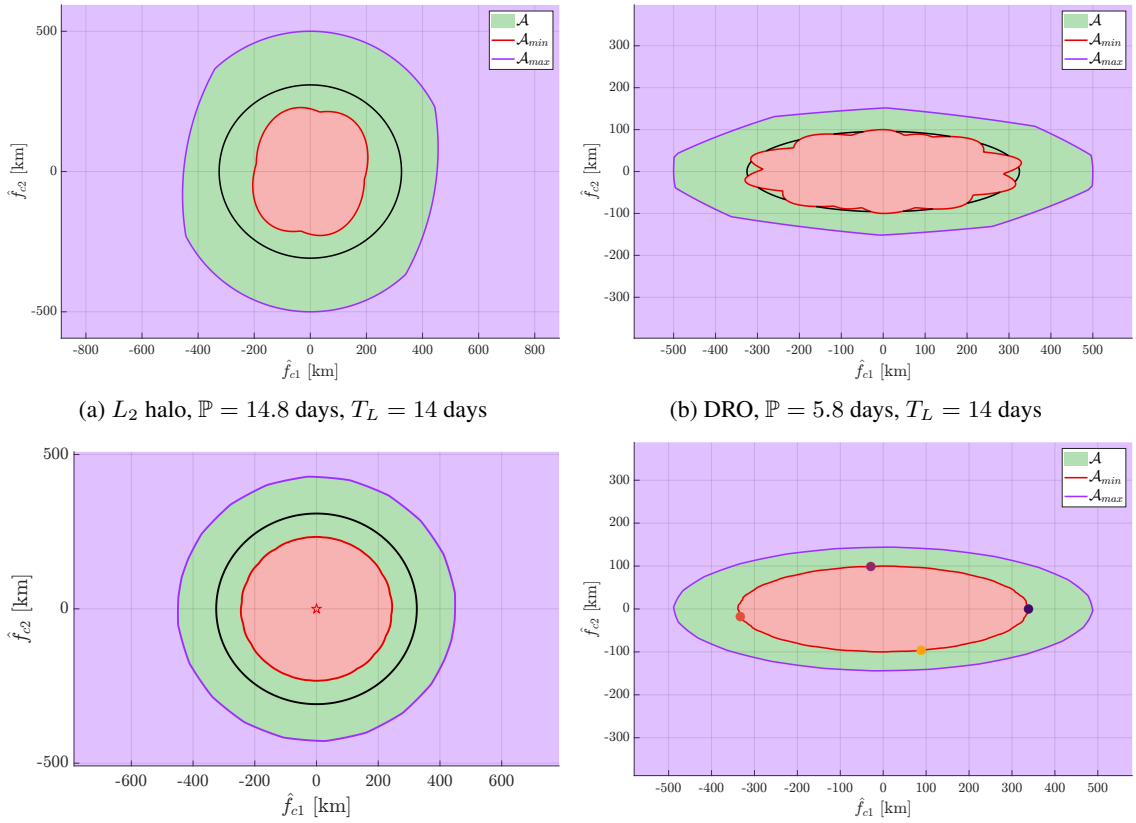

(a) L_2 halo, $\mathbb{P} = 14.8$ days, $T_L = 14$ days

(b) DRO, $\mathbb{P} = 5.8$ days, $T_L = 14$ days

(c) L_2 halo, $\mathbb{P} = 14.8$ days, $T_L = 180$ days

(d) DRO, $\mathbb{P} = 5.8$ days, $T_L = 180$ days

Figure 10: Set of acceptable solutions for $\rho_{min} = 100$ km and $\rho_{max} = 500$ km. Compliant sections of an invariant curve with semimajor axis equal to 325 km are plotted in black.

Continuation of Loitering Solutions

While the strategies for constructing loitering solutions on nearby periodic and quasiperiodic trajectories assume values for ρ_{min} and ρ_{max}, the boundary curves $\mathcal{A}_{min}$ and $\mathcal{A}_{max}$ are scaleable to reflect different

allowable separation distance envelopes. Holding loitering time constant, and assuming that $\mathcal{A}_{min}$ is constructed using ρ_{min}, a new curve ${}^{+}\mathcal{A}_{min}$ is generated corresponding to the new value ${}^{+}\rho_{min} = k\rho_{min}$ by scaling each point on the original curve by the factor k. Thus, the effect of enforcing a range of separation envelopes is observed from a single construction of $\mathcal{A}$, as in Figure 11. For a small value of ρ_{min} relative to ρ_{max}, the green region representing $\mathcal{A}$ is entirely connected, as appears in Figure 11(a) for $\rho_{min} = 25$ km and $\rho_{max} = 500$ km. However, as ρ_{min} is increased to 100 km and 250 km while holding ρ_{max} constant, the green regions become separated by the $\mathcal{A}_{min}$ curve and eventually disappear altogether, as plotted in Figures 11(b) and 11(c), respectively. It is also apparent that the ratio of ρ_{min} to ρ_{max} governs the shape of $\mathcal{A}$, rather than the absolute value of either parameter, as observed by comparing Figures 11(c) and 11(d). The plot for $\rho_{min} = 250$ km and $\rho_{max} = 500$ km is identical to the plot for $\rho_{min} = 25$ km and $\rho_{max} = 50$ km, save for the magnitude of the coordinates along each axis; both combinations of requirements yield no acceptable loitering solutions.

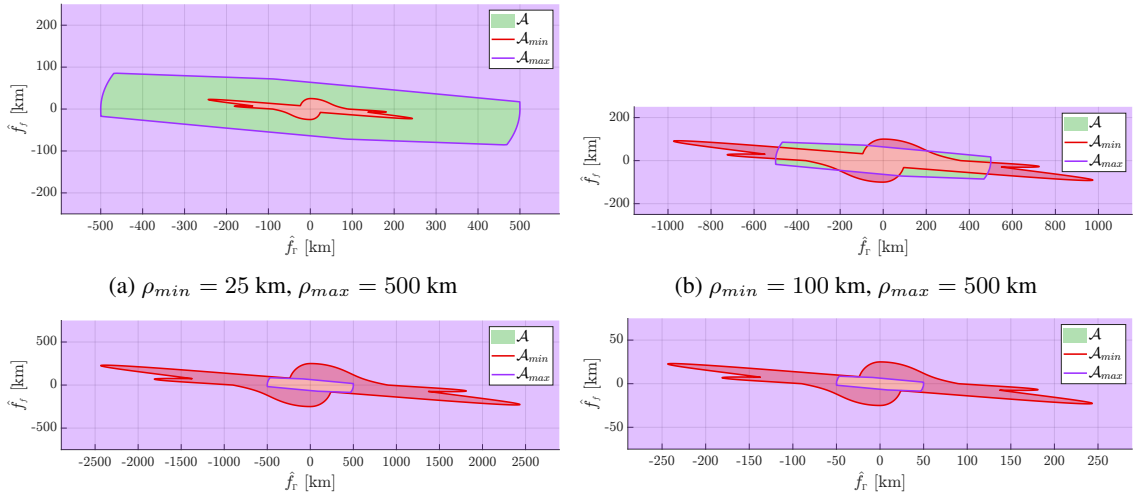

(a) $\rho_{min} = 25$ km, $\rho_{max} = 500$ km

(b) $\rho_{min} = 100$ km, $\rho_{max} = 500$ km

(c) $\rho_{min} = 250$ km, $\rho_{max} = 500$ km

(d) $\rho_{min} = 25$ km, $\rho_{max} = 50$ km

Figure 11: Effect of changing ρ_{min} for the L_1 Lyapunov $T_L = 14$ days

Loitering solutions are also available as the basis for a continuation process across loitering time. As the only requirement for solutions to lie within $\mathcal{A}$ is that the global minima and maxima lie within the range between ρ_{min} and ρ_{max}, many loitering solutions remain valid in this linear analysis for a longer T_L than initially constructed. As observable in Figure 8, trajectories that conclude the loitering phase at a separation distance other than ρ_{min} or ρ_{max} are capable of being extended while remaining compliant with the desired bounds. Figure 12 demonstrates the available surplus loitering time for two examples that both assume $\rho_{min} = 100$ km and $\rho_{max} = 500$ km: the L_2 halo orbit with an original loitering time $T_L = 180$ days, and the DRO with an original loitering time $T_L = 14$ days. Regions of solid yellow along the x-axis indicate a surplus loitering time that exceeds the bounds of the color scale. Surplus loitering time is infinite for SPF initial conditions, but the results for initial conditions where $\alpha_{f,0} \neq 0$ are dependent on the rate of phase drift for each orbit. Whereas many loitering initial conditions for the L_2 halo orbit with $\xi_t = 0.041$ are capable of being extended up to and past 180 days, the DRO examples $(\xi_t = 7.04)$ fail much earlier.

EVALUATION OF LOITERING TRAJECTORIES

After sets of acceptable initial conditions are constructed, a comparison metric is applied to aid in the selection of a single loitering trajectory. In this investigation, the comparison metric is total rendezvous cost, but different metrics are also easily applied. At the conclusion of the loitering phase, the first of two rendezvous maneuvers is initiated. These maneuvers are assumed to be impulsive, and are modeled as instantaneous changes in the spacecraft velocity. The first rendezvous maneuver is applied to the final state

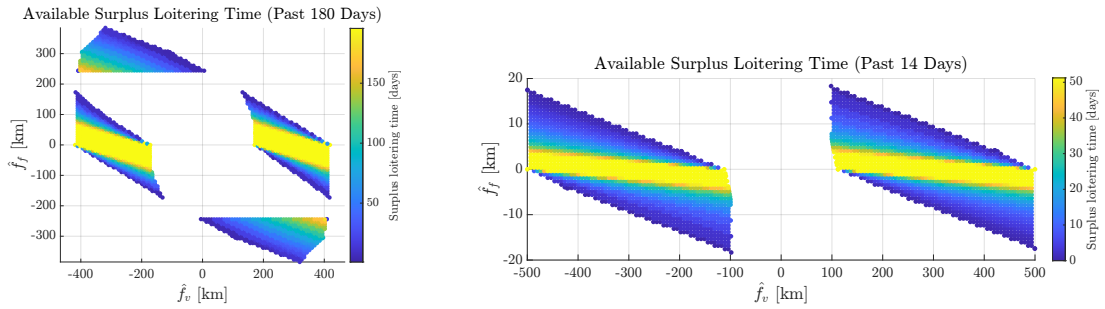

(a) L_2 halo, $T_L = 180$ days

(b) DRO, $T_L = 14$ days (y-axis enlarged)

Figure 12: Surplus Loitering Time

along each nonlinearly propagated trajectory, and all subsequent propagation during the rendezvous phase is also accomplished using the full CR3BP dynamics. At the end of the rendezvous phase, the visitor implements a second impulsive burn to achieve full state continuity with the hub. Rendezvous maneuvers are constructed by again leveraging the differential corrections and continuation methodology, and the results from constructing rendezvous conditions for a specified T_R are then evaluated for each initial condition.

Figure 13(a) demonstrates the initial (left) and final (right) conditions for the loitering phase along the L_1 Lyapunov orbit for $T_L = 14$ days. As this hub orbit lacks a complex center subspace, linear analysis predicts that long-term loitering options entirely consist of trajectories on nearby periodic trajectories. The color of each point is dictated by the total rendezvous Δv necessary to rendezvous from the end point of each loitering trajectory, where darker colors correspond to lower rendezvous costs. The trajectories and separation distance during the loitering phase, illustrated in Figure 13(b), feature an identical color scheme to Figure 13(a). From both plots in Figure 13, it is apparent that rendezvous costs tend to be lower for loitering trajectories that terminate at smaller separation distances. Additionally, the least costly solutions occur along the $\mathcal{A}_{min}$ curve as the component of the initial conditions in the x direction, i.e., the along-family component, is reduced.

Applying the results in Figure 13(a), the initial conditions that yield the least costly rendezvous for the selected T_R are available. However, a differential corrections scheme is also potentially viable to leverage the linear analysis and target the initial conditions that result in a locally optimal transfer. Applying a constraint that ensures local optimality of the converged solution, as demonstrated by McCarthy et al.,[25] the linear initial phase $(\alpha_{\Gamma,0}, \alpha_{f,0})$ that results in a linear loitering trajectory that meets the separation distance constraints and also results in the least total Δv is determined directly. The resulting initial conditions are marked in green in Figure 13(a), where it is clear that the optimal solution lies on the $\mathcal{A}_{min}$ curve. The visitor is phased to originate behind the hub on a faster periodic orbit, such that the phase drift draws the visitor near the minimum allowable separation distance when the rendezvous is initiated.

The sample L_2 halo orbit and the DRO each offer both trivial and complex center subspaces. Thus, the resulting loitering trajectories for each subspace are compared to determine the best loitering initial conditions. The initial conditions $\mathcal{A}_{min}$ and $\mathcal{A}_{max}$ are plotted in Figures 14(a) and 15(a), with the color of each point dictated by the total Δv necessary to complete a rendezvous within time of flight $T_R = 24$ hrs. Note that the scale on the y-axis for the trivial subspace in Figure 15(a) is exaggerated. For the DRO, $T_L = 14$ days, whereas $T_L = 180$ days for the halo orbit. Green markers indicate the initial conditions that result in the smallest rendezvous cost for each hub orbit; the least costly rendezvous for the L_2 halo orbit example originates from a nearby periodic trajectory, whereas the least costly rendezvous for the DRO example originates from a nearby quasiperiodic trajectory. Figures 14(b) and 15(b) represent the full trajectories originating from their respective green markers in the initial conditions plots. Initial conditions from the origin of the loitering phase are propagated *using the full CR3BP* and rendezvous maneuvers are re-targeted to ensure position continuity in the nonlinear model. In the trajectory plots, markers are placed at the originating (light purple) and terminal (magenta) points along the loitering trajectory.

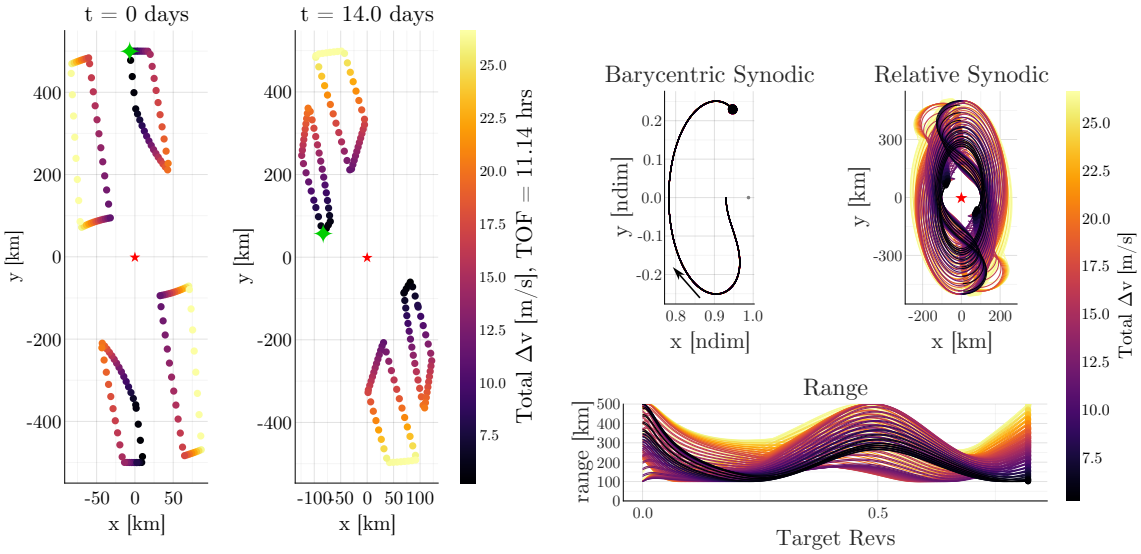

(a) Initial (left) and final (right) points for the loitering phase colored by total rendezvous Δv for $T_R = 11.1$ hrs. Points resulting in the optimal rendezvous are marked in green. (x-axis enlarged)

(b) A selection of loitering trajectories, propagated using full CR3BP dynamics, and viewed in the barycentric (left) and hub-centered (right) frames. The separation distance over the duration of the loitering phase plotted on right.

Figure 13: Loitering trajectories that meet the separation distance constraints are evaluated based on the rendezvous cost for a particular time of flight. Here, the best total rendezvous cost $\Delta v = 5.2$ m/s.

For the L_2 halo orbit, the cheapest loitering trajectory is an SPF trajectory with the visitor initialized ahead of the hub, with $\Delta v = 2.56$ m/s. As with all SPF solutions, the relative motion is perfectly periodic in both the barycentric and relative frames, as illustrated in Figure 14(b). Note that while similar "teardrop" trajectories are constructed by leveraging Floquet mode control,[12] the distinctive shape simply arises by projecting trivial subspace motion in the halo family onto the x-y plane. For non-SPF loitering within the trivial subspace, the initial conditions that yield the cheapest rendezvous costs lie along the portions of the $\mathcal{A}_{min}$ curve where the along-track phase drift for the visitor brings it closer to the hub, as in the Lyapunov example. This behavior is demonstrated by the blue trajectory in Figure 8(a). Alternatively, the most expensive loitering options are those similar to the green trajectory in Figure 8(a), which lie on the $\mathcal{A}_{max}$ curve and never approach the minimum allowable separation distance. Overall, the Δv ranges from 2.56 to 6.65 m/s along the $\mathcal{A}_{min}$ curve and from 3.22 to 6.90 m/s along the $\mathcal{A}_{max}$ curve. The rendezvous costs from loitering by exploiting quasiperiodic motion, meanwhile, are much more consistent along the boundaries of acceptable initial conditions. The Δv for rendezvous from the $\mathcal{A}_{min}$ curve ranges from 3.27 to 3.44 m/s, and the outer curve renders costs between 6.05 and 6.34 m/s. While no QPO solution is superior to the best solutions from the trivial subspace, the geometry of the QPOs in the vicinity of the hub orbit indicates that loitering on the smallest possible torus matters much more than the placement in a specific phase along the torus for this particular example.

In the case of the DRO, the cheapest loitering solution is a QPO trajectory, as plotted in Figure 15(b). Because of the relatively high value of ξ_t for this hub orbit, the area of the $\mathcal{A}$ region within the trivial subspace is much smaller than within the complex center subspace. The trends for trivial subspace solutions from the L_2 halo and L_1 Lyapunov examples hold, where rendezvous costs decrease for solutions where phase drift forces the visitor closer to the hub. For the trivial subspace, rendezvous Δv ranges between 2.21 and 12.82 m/s, with the cheapest solutions again occurring along the $\mathcal{A}_{min}$ curve. Rendezvous costs from quasiperiodic loitering orbits, in contrast to the halo, have a larger range of values of Δv, from 2.12 m/s to 12.48 m/s. As the invariant curve for the DRO is very eccentric, phasing within the complex center subspace has a large influence on rendezvous costs. Separation distance at the end of the loitering phase for the best QPO solution is minimized.

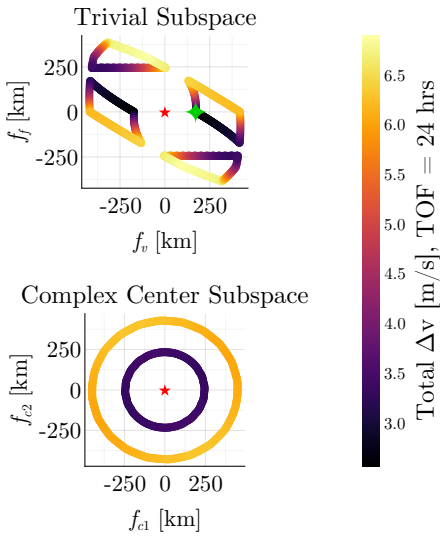

(a) Initial conditions colored by Δv

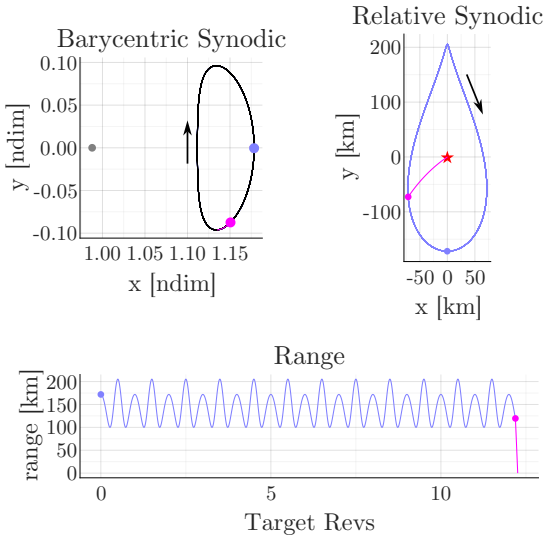

(b) SPF trajectory, propagated using full CR3BP dynamics, that yields the most cost effective rendezvous. Originating and terminal points of the loitering phase marked in light purple and magenta, respectively.

Figure 14: Comparison of $T_L = 180$ day loitering solutions using rendezvous Δv for the L_2 halo

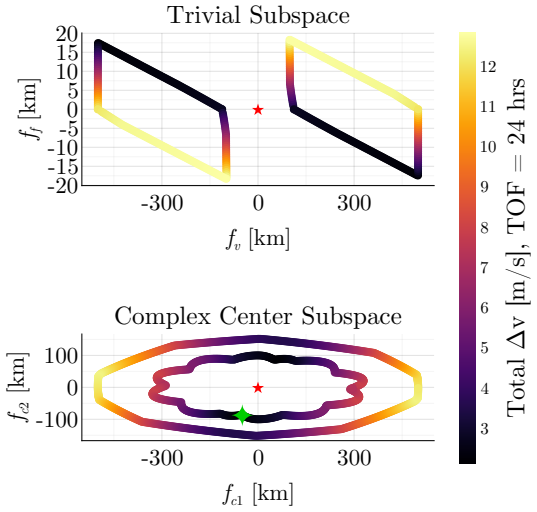

(a) Initial conditions colored by Δv (y-axis enlarged)

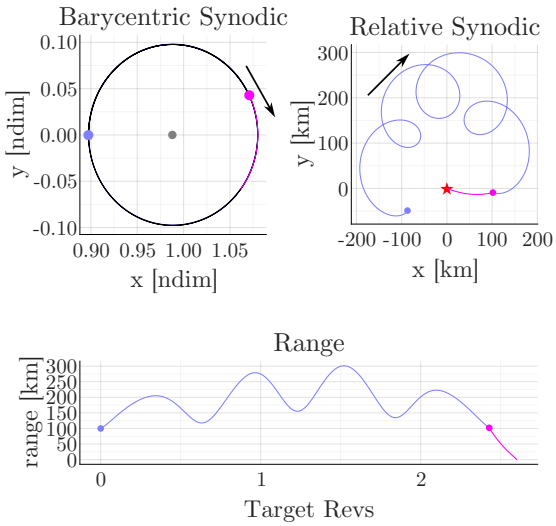

(b) QPO trajectory, propagated using full CR3BP dynamics, that yields the most cost effective rendezvous. Originating and terminal points of the loitering phase marked in light purple and magenta, respectively.

Figure 15: Comparison of $T_L = 14$ day loitering solutions using rendezvous Δv for the DRO

Although the sets of loitering conditions contained within the $\mathcal{A}$ region are constructed by leveraging linear

dynamics, nonlinear trajectories propagated directly from the linearly generated solutions retain the expected characteristics for the relative motion. The percent error in position components for the three examples discussed in this section appears in Figure 16. The loitering problem is particularly suitable for linear analysis, as the separation distances are small, resulting in solutions that are likely to remain within the range of validity for the linear approximation. Additionally, linear solutions are propagated using the Floquet decomposition such that the unstable modes are removed. Nonlinear solutions, meanwhile, are propagated from initial conditions on converged periodic and quasiperiodic orbits that correspond to the desired initial conditions. Thus, the initial error is not necessarily zero, but both linear and nonlinear propagations remain very accurate (below 0.5% error) for long propagation times on the unstable orbits.

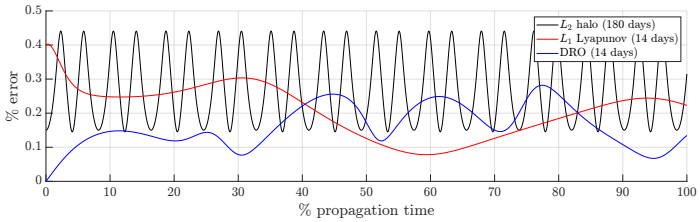

Figure 16: Percent error between linear and nonlinear propagations

SUMMARY

In this investigation, a preliminary design methodology for constructing long-term cislunar loitering orbits, subject to constraints on minimum and maximum separation distance, is introduced. Loitering design is demonstrated with the use of three sample hub orbits, an L_2 halo orbit, an L_1 Lyapunov orbit, and a DRO, that possess varying geometries, locations within cislunar space, and stability characteristics. Linearized CR3BP dynamics, formulated using the Floquet modal decomposition, are leveraged to target sets of initial conditions that lie on the edges of the desired separation distance envelope. Solutions lying in the trivial and complex center subspaces are treated as separate targeting problems. Acceptable loitering conditions are demonstrated to remain within the desired separation envelope past the original loitering period, and the boundaries for the sets of acceptable initial conditions are scaled to meet changes in the requirements to the minimum or maximum allowable separation distances. Long loitering times are achieved with this strategy, regardless of the stability of the hub orbit.

Once loitering initial conditions are constructed, the cost of completing a rendezvous from the terminal state of the loitering phase is leveraged as the metric to evaluate each solution. The loitering orbit that leads to the lowest rendezvous cost is selected for advancement into the full nonlinear CR3BP dynamics. For hub orbits that possess both trivial and complex center subspaces, the rendezvous cost metric is applied to determine the subspace that possesses the most desirable characteristics. The initial conditions from the linear targeting process transition well to the nonlinear CR3BP, with low position errors relative to the separation distance bounds. At the conclusion of the preliminary loitering design process, the results are available for further optimization and transition to a high-fidelity ephemeris model to complete the design process.

ACKNOWLEDGEMENTS

The authors would like to thank the Purdue University School of Aeronautics and Astronautics for providing the financial support necessary to perform this work. The authors would also grateful to their fellow members of the Purdue Multi-Body Dynamics Research Group for countless insightful suggestions and discussions.

REFERENCES

[1] A. J. Cavaciuti, J. H. Heying, and J. Davis, “In-Space Servicing, Assembly, and Manufacturing for the New Space Economy,” Center for Space Policy and Strategy, July 2022.

[2] National Aeronautics and Space Administration, "Gateway Space Station - NASA," Mar. 2024. Section: Humans in Space.

[3] J. C. Crusan, R. M. Smith, D. A. Craig, J. M. Caram, J. Guidi, M. Gates, J. M. Krezel, and N. B. Herrmann, "Deep space gateway concept: Extending human presence into cislunar space," *2018 IEEE Aerospace Conference*, Mar. 2018, pp. 1–10, 10.1109/AERO.2018.8396541.

[4] National Aeronautics and Space Administration, "NASA 2022 Strategic Plan," 2022.

[5] T. L. Team, "The LUVOIR Mission Concept Study Final Report," Dec. 2019. arXiv:1912.06219 [astro-ph], 10.48550/arXiv.1912.06219.

[6] I. Elliott and N. Bosanac, "Describing relative motion near periodic orbits via local toroidal coordinates," *Celestial Mechanics and Dynamical Astronomy*, Vol. 134, Apr. 2022, p. 19, 10.1007/s10569-022-10074-8.

[7] I. Elliott and N. Bosanac, "Spacecraft Formation Control Near a Periodic Orbit Using Geometric Relative Coordinates," *AAS/AIAA Spaceflight Mechanics Meeting*, Virtual, Feb. 2021, p. 20.

[8] D. B. Henry and D. J. Scheeres, "Expansion Maps: Designing Relative Trajectories on Quasi-Periodic Orbits," *Journal of Guidance, Control, and Dynamics*, Vol. 44, Mar. 2021, pp. 457–468, 10.2514/1.G005492.

[9] E. R. Burnett and H. Schaub, "Spacecraft Relative Motion Dynamics and Control Using Fundamental Modal Solution Constants," *Journal of Guidance, Control, and Dynamics*, Aug. 2022, pp. 1–14, 10.2514/1.G006603.

[10] B. T. Barden and K. C. Howell, "Fundamental Motions Near Collinear Libration Points and Their Transitions," *The Journal of the Astronautical Sciences*, Vol. 46, Dec. 1998, pp. 361–378.

[11] B. T. Barden and K. C. Howell, "Dynamical Issues Associated with Relative Configurations of Multiple Spacecraft Near the Sun-Earth/Moon L1 Point," *AAS/AIAA Astrodynamics Specialist Conference*, Girdwood, Alaska, Aug. 1999, p. 20.

[12] K. C. Howell and B. G. Marchand, "Natural and non-natural spacecraft formations near the L1 and L2 libration points in the Sun–Earth/Moon ephemeris system," *Dynamical Systems*, Vol. 20, Mar. 2005, pp. 149–173, 10.1080/14689360420002982 24.

[13] M. Duering, M. Vasile, and M. Landgraf, "Uncontrolled Spacecraft Formations on Two-Dimensional Invariant Tori," Pasadena, California, Oct. 2012.

[14] G. Gómez, M. Marcote, J. J. Masdemont, and J. M. Mondelo, "Zero Relative Radial Acceleration Cones and Controlled Motions Suitable for Formation Flying," *The Journal of the Astronautical Sciences*, Vol. 53, Dec. 2005, pp. 413–431, 10.1007/BF03546361.

[15] A. Héritier and K. C. Howell, "Dynamical evolution of natural formations in libration point orbits in a multi-body regime," *Acta Astronautica*, Vol. 102, Sept. 2014, pp. 332–340, 10.1016/j.actaastro.2013.10.017.

[16] F. J. T. Salazar, J. J. Masdemont, G. Gómez, E. E. Macau, and O. C. Winter, "Zero, minimum and maximum relative radial acceleration for planar formation flight dynamics near triangular libration points in the Earth–Moon system," *Advances in Space Research*, Vol. 54, Nov. 2014, pp. 1838–1857, 10.1016/j.asr.2014.07.018.

[17] D. Zuehlke and T. Henderson, "Periodic Relative Natural Motion in the Circular Restricted Three-Body Problem," *33rd AAS/AIAA Space Flight Mechanics Meeting*, Austin, Texas, Jan. 2023.

[18] F. Khoury and K. C. Howell, "Orbital Rendezvous and Spacecraft Loitering in the Earth-Moon System," *AAS/AIAA Astrodynamics Specialist Conference*, Lake Tahoe, California, Aug. 2020, p. 20.

[19] C. Sandel and R. Sood, "Natural and Forced Spacecraft Loitering in a Near Rectilinear Halo Orbit," *The Journal of the Astronautical Sciences*, Vol. 71, May 2024, p. 28, 10.1007/s40295-024-00446-7.

[20] W. Wiesel and D. Pohlen, "Canonical Floquet theory," *Celestial Mechanics and Dynamical Astronomy*, Vol. 58, Oct. 1994, pp. 81–96, 10.1007/BF00692119.

[21] V. A. Yakubovich and V. M. Starzhinskii, *Linear Differential Equations with Periodic Coefficients*, Vol. 1. Wiley, 1975.

[22] G. Gómez and J. Mondelo, "The dynamics around the collinear equilibrium points of the RTBP," *Physica D: Nonlinear Phenomena*, Vol. 157, Oct. 2001, pp. 283–321, 10.1016/S0167-2789(01)00312-8.

[23] Z. P. Olikara and D. J. Scheeres, "Numerical Method for Computing Quasi-Periodic Orbits and their Stability in the Restricted Three-Body Problem," *Advances in the Astronautical Sciences*, Vol. 145, 2012, pp. 911–930.

[24] B. P. Mccarthy and K. C. Howell, "Leveraging quasi-periodic orbits for trajectory design in cislunar space," *Astrodynamics*, Vol. 5, No. 2, 2021, pp. 139–165, 10.1007/s42064-020-0094-5.

[25] B. McCarthy, S. Scheuerle, E. Zimovan-Spreen, D. Davis, and K. Howell, "Rephasing and Loitering Strategies in the Gateway Near Rectilinear Halo Orbit," Big Sky, Montana, Aug. 2023.